

## Midlatitude Cirrus Clouds Derived from Hurricane Nora: A Case Study with Implications for Ice Crystal Nucleation and Shape

KENNETH SASSEN,\* W. PATRICK ARNOTT,<sup>†</sup> DAVID O'C. STARR,<sup>#</sup> GERALD G. MACE,<sup>@</sup> ZHIEN WANG,& AND  
MICHAEL R. POELLOT\*\*

*\*Geophysical Institute, University of Alaska, Fairbanks, Fairbanks, Alaska*

*<sup>†</sup>Desert Research Institute, Reno, Nevada*

*<sup>#</sup>NASA Goddard Space Flight Center, Greenbelt, Maryland*

*<sup>@</sup>Department of Meteorology, University of Utah, Salt Lake City, Utah*

*&University of Maryland, Baltimore County, Baltimore, Maryland*

*\*\*Atmospheric Sciences Department, University of North Dakota, Grand Forks, North Dakota*

(Manuscript received 18 March 2002, in final form 27 August 2002)

### ABSTRACT

Hurricane Nora traveled up the Baja Peninsula coast in the unusually warm El Niño waters of September 1997 until rapidly decaying as it approached southern California on 24 September. The anvil cirrus blowoff from the final surge of tropical convection became embedded in subtropical flow that advected the cirrus across the western United States, where it was studied from the Facility for Atmospheric Remote Sensing (FARS) in Salt Lake City, Utah, on 25 September. A day later, the cirrus shield remnants were redirected southward by midlatitude circulations into the southern Great Plains, providing a case study opportunity for the research aircraft and ground-based remote sensors assembled at the Clouds and Radiation Testbed (CART) site in northern Oklahoma. Using these comprehensive resources and new remote sensing cloud retrieval algorithms, the microphysical and radiative cloud properties of this unusual cirrus event are uniquely characterized.

Importantly, at both the FARS and CART sites the cirrus generated spectacular halos and arcs, which acted as a tracer for the hurricane cirrus, despite the limited lifetimes of individual ice crystals. Lidar depolarization data indicate widespread regions of uniform ice plate orientations, and in situ particle replicator data show a preponderance of pristine, solid hexagonal plates and columns. It is suggested that these unusual aspects are the result of the mode of cirrus particle nucleation, presumably involving the lofting of sea salt nuclei in strong thunderstorm updrafts into the upper troposphere. This created a reservoir of haze particles that continued to produce halide-salt-contaminated ice crystals during the extended period of cirrus cloud maintenance. The inference that marine microbiota are embedded in the replicas of some ice crystals collected over the CART site points to the longevity of marine effects. Various nucleation scenarios proposed for cirrus clouds based on this and other studies, and the implications for understanding cirrus radiative properties on a global scale, are discussed.

### 1. Introduction

Cirrus clouds are formed through a variety of weather processes that inject water vapor into the upper troposphere, which in turn suffers dehydration and cloud-forming aerosol cleansing through the subsequent precipitation of the ice particles produced during cirrus growth and maintenance (Sassen 2002a). Since cirrus-producing weather patterns may vary significantly with season and latitude (Sassen and Campbell 2001), it is reasonable to assume that basic cirrus properties will depend substantially on geography. For example, synoptic-scale disturbances associated with jet streams would be primarily responsible for cirrus at most mid-

latitude locations, whereas opportunities to study the cirrus cloud blowoff from organized tropical convection would be infrequent. Nonetheless, although a minor contributor to midlatitude cirrus, such tropical cirrus are abundant in regions of the globe that, unfortunately, generally still lack sophisticated remote sensing or in situ research capabilities.

A rare opportunity to comprehensively study cirrus clouds derived from organized tropical convection occurred near the end of September 1997, as Hurricane Nora swept up the Baja Peninsula coast, nurtured by the unusually warm El Niño waters in the eastern Pacific Ocean. Soon after crossing the Baja Peninsula as a hurricane on the morning of 25 September, Nora entered the southwestern United States at ~2100 UTC as a tropical storm. Total storm rainfall amounts of 10–15 cm were common in southern Arizona, while Death Valley, California, received 2.8 cm. Considerable damage to

---

*Corresponding author address:* Kenneth Sassen, Geophysical Institute, University of Alaska, Fairbanks, P.O. Box 757320, Fairbanks, AK 99775.  
E-mail: ksassen@gi.alaska.edu

agriculture in Arizona, widespread power outages in California, and damage to forests in the mountains of southern Utah were attributed to this storm. Meanwhile, the decaying depression ejected inland a massive cirrus cloud shield that would soon traverse much of North America. Over this period the cirrus would be studied from the Facility for Atmospheric Remote Sensing (FARS; Sassen et al. 2001) in Salt Lake City, Utah, and the Southern Great Plains Clouds and Radiation Testbed (SGP CART; Stokes and Schwartz 1994) site near Lamont, Oklahoma, where, serendipitously, a major cloud experiment—supported by ground-based polarization and Raman lidars, a millimeter-wave Doppler radar, and research aircraft—was taking place.

An interesting aspect of this incursion of tropical cirrus into the continental United States is that spectacular optical displays were associated with the cirrus observed at both the FARS and SGP CART sites (and likely elsewhere). The components included the common  $22^\circ$  halo with tangent arcs, parhelia of  $22^\circ$  and  $120^\circ$ , and a parhelic circle. However, assuming, for example, that 200- $\mu\text{m}$ -diameter oriented plate or thick plate crystals contributed to the displays, the corresponding 0.1–0.2  $\text{m s}^{-1}$  fall speeds (Pruppacher and Klett 1997) indicate that such particles would fall through a cloud depth of 1 km in a 1.5–3-h period in the absence of dynamic recycling effects. Thus, there is little question that the entire population of ice crystals was replaced (many times over) during the cirrus transport to the central United States. Yet, a similar halo/arc complex was observed over the about 30-h period between the observations at the FARS and SGP CART sites.

We consider it important to account for this persistence in optical displays, for it suggests that cirrus ice crystal shapes (and hence radiative properties) display a dependence on the cloud formation mechanism, or more fundamentally because of the age of these clouds, on the manner of ice nucleation and the ice phase chemistry during subsequent crystal growth. Current knowledge indicates that cirrus particle formation occurs predominantly through the freezing in updrafts of haze particles derived from cloud condensation nuclei (CCN) within the homogeneous freezing domain at temperatures  $< -38^\circ\text{C}$  (Sassen and Dodd 1988; Pruppacher and Klett 1997), although the relative role played by ice nuclei (IN) is still unclear (DeMott et al. 1998). Midlatitude cirrus cloud particle-forming CCN are believed to be usually associated with inorganic ionizable salts such as ammonium sulfate, bisulfate, and nitrate, or, alternatively, aqueous sulfuric acid droplets (Tabazadeh and Toon 1998; Chen et al. 2000). The ammonium sulfate particles commonly present in the upper troposphere may be derived either from the boundary layer or the stratosphere after sulfuric acid droplet neutralization via ammonium gas absorption (Sassen et al. 1995).

However, it is apparent that the majority of documented cirrus studies reflect a midlatitude continental

bias, suggesting that the major climatic impact (in terms of global coverage) of CCN convectively derived from the surface of the oceans is underappreciated. These nuclei involve mainly chloride salts of sodium and magnesium, and other trace substances. It has been shown in the laboratory that sea salt nuclei act as a contaminant to ice crystal growth after nucleation, thereby affecting ice crystal morphology (Finnegan and Pitter 1997). After examining the Nora case in terms of the synoptic setting and remote sensing and in situ measurements, we consider the hypothesis that cirrus cloud content and radiative properties are affected by the cloud forming particles that are brought to cirrus cloud altitudes by various weather processes.

## 2. Instrumentation

This case study is unique in that the same cirrus cloud system was studied from two advanced remote sensing facilities about 1400 km and 1 day apart. The first site, FARS, is located at  $40^\circ49'00''\text{N}$  and  $111^\circ49'38''\text{W}$ , while the SGP CART site is at  $36^\circ36'18''\text{N}$  and  $97^\circ26'06''\text{W}$ . Because a major cloud experiment was taking place at the CART site, much of the instrumentation normally stationed at FARS was transported to the CART site during this period. A thorough description of FARS equipment has recently been given in Sassen et al. (2001), so only brief descriptions of the lidars are given below.

Remaining at FARS was the cloud polarization lidar (CPL), which is based on a ruby (0.694  $\mu\text{m}$ ) laser transmitter with a 1.5-J output and a pulse repetition frequency of 0.1 Hz. The backscattered powers in the planes of polarization orthogonal and parallel to the (vertically polarized) laser are digitized at a 7.5-m range resolution, from which linear depolarization ratios ( $\delta$ ) are derived. Although normally vertically pointing, the lidar table is manually steerable  $\sim \pm 5^\circ$  from the zenith direction to identify the backscattering anisotropy caused by horizontally oriented ice crystals, and so also to unambiguously identify liquid cloud layers (Sassen and Benson 2001). The mobile polarization diversity lidar (PDL) then deployed at the CART site is a considerably more sophisticated dual-wavelength (0.532 and 1.06  $\mu\text{m}$ ) device based on an Nd:YAG laser transmitter with 0.35-J outputs in each color and a 10-Hz pulse rate. Data is digitized at range intervals down to 1.5 m. Although both receivers (one for each color) measure  $\delta$  values, during the supporting aircraft mission, data were only collected in the 0.532- $\mu\text{m}$  channels. Moreover, because of pilot eye safety issues, no scanning operations were conducted even though the lidar is fully scannable.

Permanent equipment utilized here from the SGP CART site include the millimeter-wave cloud radar (MMCR) and the CART Raman lidar. The MMCR is a vertically pointing K-band (9.6 mm) Doppler radar with 75-m range resolution, which is uniquely suited to detect

cirrus clouds (Moran et al. 1998). Calibration of the equivalent radar reflectivity factor  $Z_e$  ( $\text{mm}^6 \text{m}^{-3}$ ) is considered to be better than 2 dB based on radar intercomparison research. The advanced design of the CART Raman lidar has been described in Goldsmith et al. (1998), and includes several elastic and inelastic channels for molecular nitrogen and water vapor, particle backscattering and depolarization. The ability to relate the retrieved nitrogen concentrations to those derived from sounding-based air density profiles allows this system to inherently determine the extinction coefficients caused by cirrus particles. However, the much higher resolution PDL is relied on here to provide the lidar returned power and depolarization displays.

The Citation aircraft from the University of North Dakota (UND) has a sufficient ceiling altitude to reach most midlatitude cirrus cloud tops. It was equipped with a standard set of parameter of state, vertical motion, and cloud microphysical probes, the latter including the 2D-C probe as well as an ice crystal replicator provided by the Desert Research Institute (Arnott et al. 1994). The mission consisted basically of a series of step-up or step-down legs combined with Eulerian spirals to obtain vertical profiles of cloud content as close to the CART site as possible. The horizontal legs were 10–20 km in length, whereas the spiral ascents/descents were  $\sim 10$  km in diameter: both the edges of the legs and spirals were anchored vertically over the CART site.

In view of the labor intensive analysis of the replicator data (before the tape ran out at 1912 UTC), the goal was to obtain representative images of all crystal types observed in nominal 10-s time intervals, corresponding to  $\sim 1.4$  km of cloud sample. Much of this analysis can be accessed online (see [http://www.dri.edu/Projects/replica/DOE.ARM/doearm97iop/09\\_26\\_97case/09\\_26\\_97case.html](http://www.dri.edu/Projects/replica/DOE.ARM/doearm97iop/09_26_97case/09_26_97case.html)), which supplements the data given here. The 10-s intervals were usually adequate to count and size a representative ensemble of crystals, whereas details of the size spectra began to be lost on longer time intervals.

### 3. Synoptic weather setting

The cirrus clouds observed over northern Utah and Oklahoma on 25 and 26 September 1997, respectively, were associated with upper tropospheric outflow from Hurricane Nora and its remnants. Hurricane Nora developed rapidly from a tropical depression over the eastern Pacific on 16 September and deepened into a tropical storm a day later, and finally into a hurricane on 18 September. The system reached a peak wind intensity of  $60 \text{ m s}^{-1}$  with a central pressure of 950 mb over the anomalously warm ( $29^\circ\text{--}30^\circ\text{C}$ ) El Niño waters near  $17^\circ\text{N}$ ,  $108^\circ\text{W}$ . Ahead of a broad, nearly stationary trough along  $125^\circ\text{W}$  on 23 September, there was southerly flow at all levels from the intertropical convergence zone (ITCZ) northward into the western mountains of North America. Another prominent synoptic feature was the midtropospheric ridge along the spine of the Rocky

Mountains from Mexico into southern Canada. This pattern resembled a weak blocking ridge.

Hurricane Nora became entrained in the southerly flow and accelerated northward along the Baja Peninsula on 23 September. The evolution of the large-scale meteorology during this period is shown in Fig. 1, derived from the National Centers for Environmental Prediction (NCEP) reanalysis (Kalnay et al. 1996). On 24 September, the lower tropospheric circulation associated with Nora, clearly visible in the satellite imagery (Fig. 2, top), was not well resolved by the reanalysis (Fig. 1, top). However, the large-scale vertical motion at 250 mb shows a broad area of upward motion ( $>3 \text{ cm s}^{-1}$ ) associated with upper tropospheric divergence and the large-scale tropical circulation in which Nora was embedded. During this period, as Nora transited northward along the Baja coast, the cirrus outflow from the weakening system advected into southern Arizona and New Mexico. The outflow is particularly evident in the NCEP upper tropospheric humidity field where a corresponding belt of enhanced humidity extends into east Texas at 1200 UTC 24 September.

On 25 September, Nora turned northeastward over Baja and the circulation appeared to become disorganized (Fig. 2, middle). The upper tropospheric vertical motion that resulted in the previously extensive cirrus outflow waned somewhat, but then reintensified by 1200 UTC 25 September with peak values of  $7 \text{ cm s}^{-1}$  over southern California. The NCEP reanalysis suggests, and satellite imagery confirms, that a cirrus shield was injected into the upper troposphere within and downstream of this region of ascent. By 1800 UTC 25 September, this cloud shield covered much of the intermountain western United States. The 500-mb ridge axis was now oriented north–south along  $\sim 103^\circ\text{W}$ . At this time cirrus were being observed by remote sensors at the University of Utah FARS site (see section 4), in a layer based at  $\sim 8.0$  km at 1700 UTC. The layer progressively thickened until it became optically thick enough to be visually identified as altostratus after  $\sim 2000$  UTC. It is worth noting the good correspondence between the region of high relative humidity resolved by the NCEP analysis (1200 UTC) and the upper tropospheric clouds in the satellite imagery (0600 and 1800 UTC) on 25 September. The cirrus were associated with the ascending air over the intermountain United States, but apparently advected into a region of large-scale descent where the clouds thinned as they approached the ridge axis.

The pattern in the middle and upper troposphere became somewhat more progressive on 26 September as a short-wave trough approached the Pacific Northwest. The ridge axis at 500 mb began to tilt and then move eastward. By 1200 UTC, the 500-mb ridge axis passed northeastward through the Oklahoma panhandle. The ARM site was still in weak northwesterly flow of  $\sim 25 \text{ m s}^{-1}$  at 300 mb at midday on 26 September, indicating that the ridge axis at this level was still to the west. As



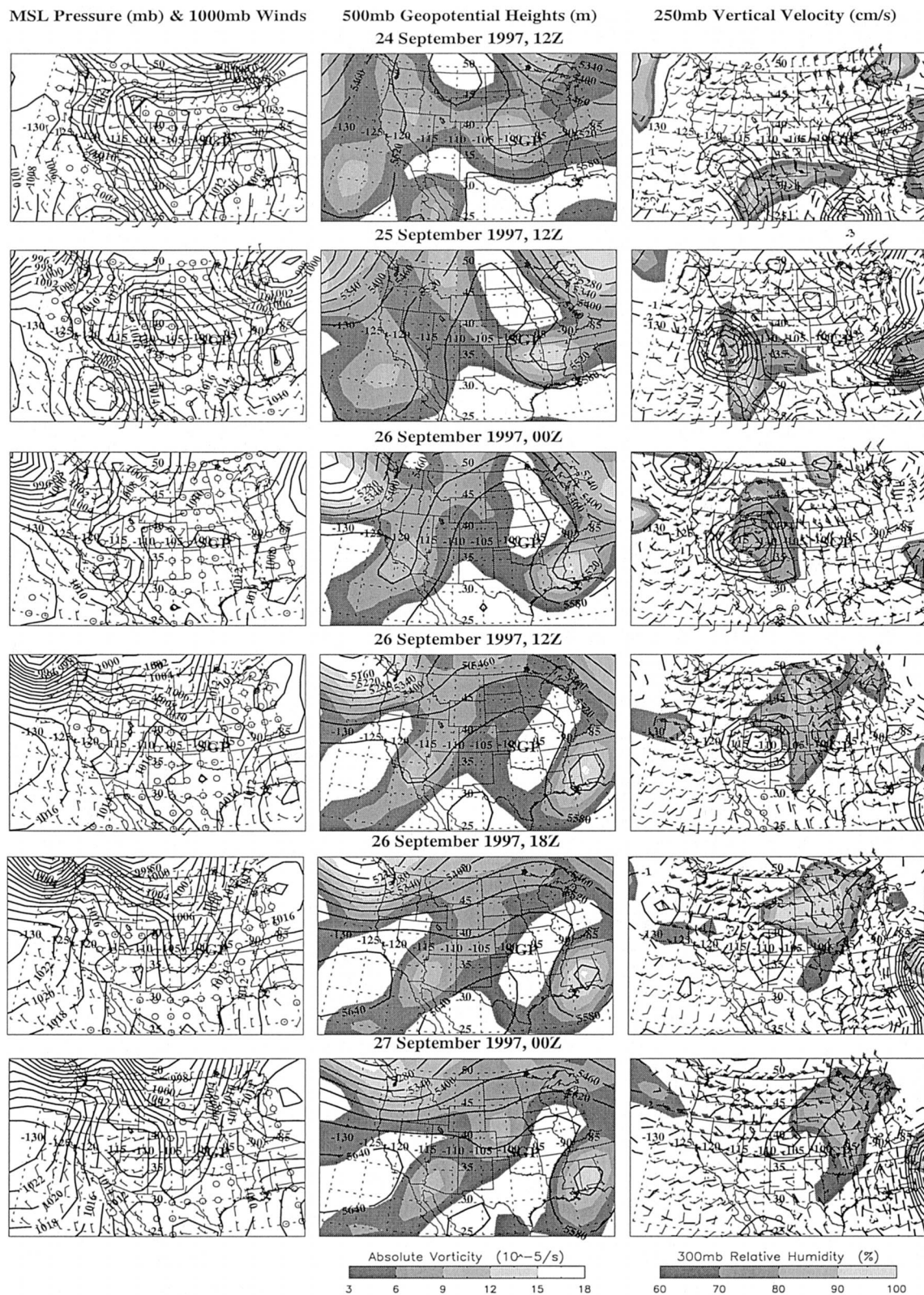


FIG. 1. Evolution of the indicated synoptic weather conditions following the decay of Hurricane Nora, derived from NCEP reanalyses. Wind barbs are in  $10 \text{ m s}^{-1}$  intervals for the full ticks. Grayscales for absolute vorticity and relative humidity are inserted at bottom.



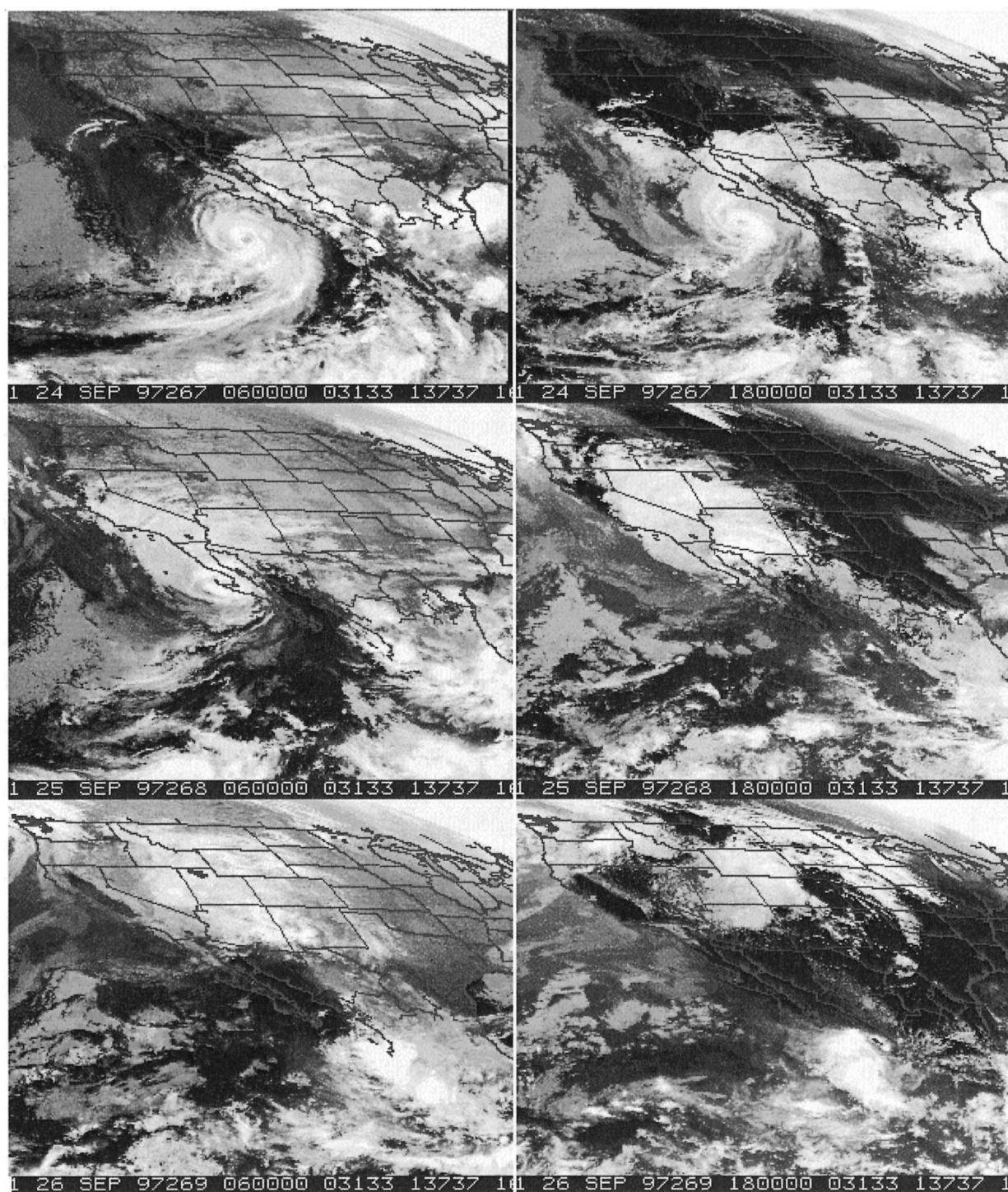


FIG. 2. Sequence of 12-hourly GOES infrared channel views of the western United States showing the decay of Hurricane Nora and the spread of the cirrus cloud shield across the southwest on 24 Sep, the University of Utah FARS site on 25 Sep, and the SGP CART site on 26 Sep 1997.

the pattern deamplified and became progressive, the reanalysis suggests that the ascent weakened in the upper troposphere, although an extensive region downwind of the vertical motion maximum continued to exhibit el-

evated values of upper tropospheric relative humidity (Fig. 1).

Three-hourly radiosonde observations at the SGP CART site (Fig. 3) show increasing upper tropospheric

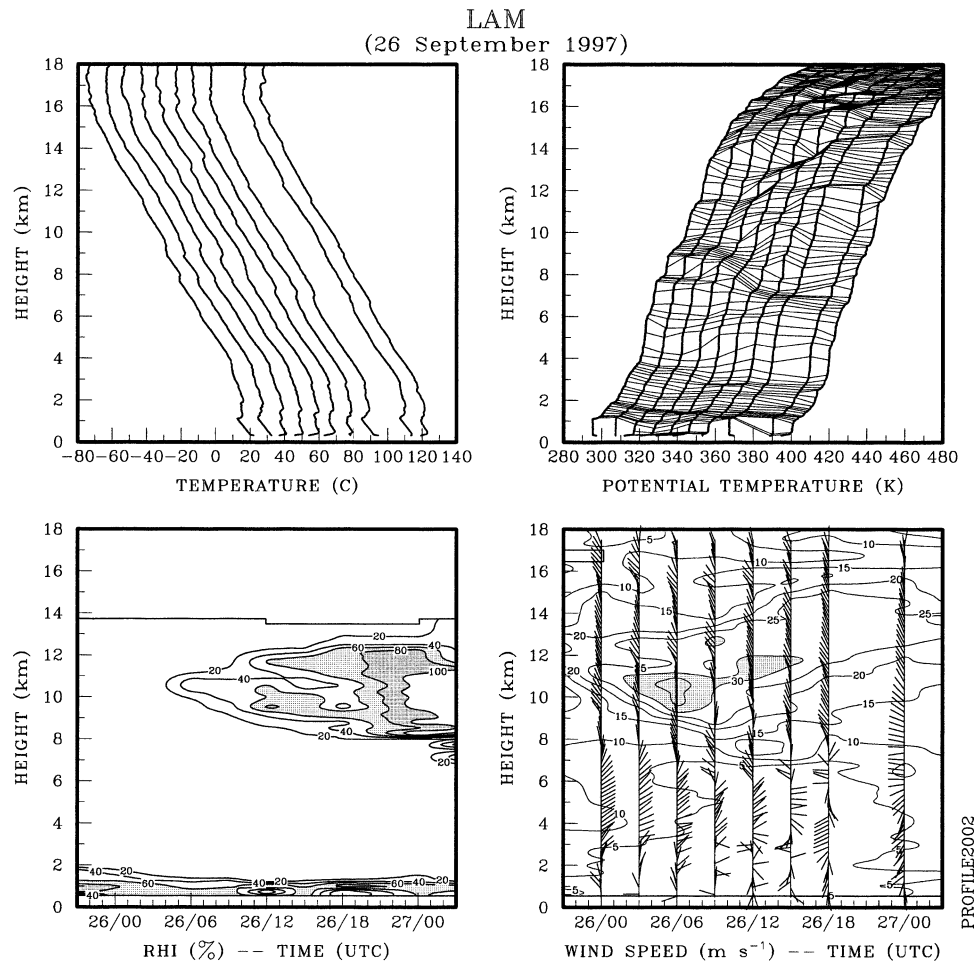


FIG. 3. Time sequence of 3-hourly radiosonde observations from the SGP CART site near Lamont (LAM), OK, over the period of 2100 UTC 25 Sep to 0300 UTC 27 Sep 1997. Vertical profiles of (top left) temperature (progressively offset by 10°C) and (top right) potential temperatures (offset by 10 K). (bottom left) A time–height analysis of relative humidity (via standard processing but converted to *with respect to ice* at upper levels). (bottom right) A time–height isotach wind analysis, where wind direction is indicated by constant-length barbs. The variable wind directions at low levels are associated with very light winds.

moisture in a layer near 11 km beginning at 0600 UTC on 26 September, later bifurcating into two layers of enhanced humidity around 9 km and from 11 to 12 km, and then developing into a deep moist layer from 8 to 12.5 km by 0000 UTC. A north–south-oriented cirrus band, located just downstream of the ridge axis, approached the CART site at ~1800 UTC (Fig. 4). Contrail formation was observed within the main cloud band and in the moist westerly flow to the west (Duda et al. 2001). Over the next 3 h, as the Citation conducted a mission in the cirrus band, the north–south-oriented cirrus band progressed slowly eastward and passed over the CART site. By 0000 UTC 27 September, the ridge axis passed to the east as the upper-tropospheric flow turned westerly (Fig. 3). Interestingly, the data suggest that large-scale descending air persisted in the upper troposphere during this entire cloud event. A similar

finding was reported by Starr and Wylie (1990) in “ridge-crest” cirrus.

It is of note that the stable, dry, midtropospheric air over the CART site on 26 September resembled an elevated frontal zone (the region of closely spaced isentropes in Fig. 3) at ~7.0 km after 1200 UTC. The overrunning Hurricane Nora air is characterized by reduced static stability (wider separation of the isentropes in Fig. 3), especially from 10 to 12 km at 0000 UTC on 27 September, and is capped by a more stable region that extends from 12 km to about 16 km where the lapse rate becomes distinctly stratospheric.

#### 4. The FARS dataset

Figure 5 provides an overview of the cirrus conditions observed from FARS over the 1600–2030 UTC obser-



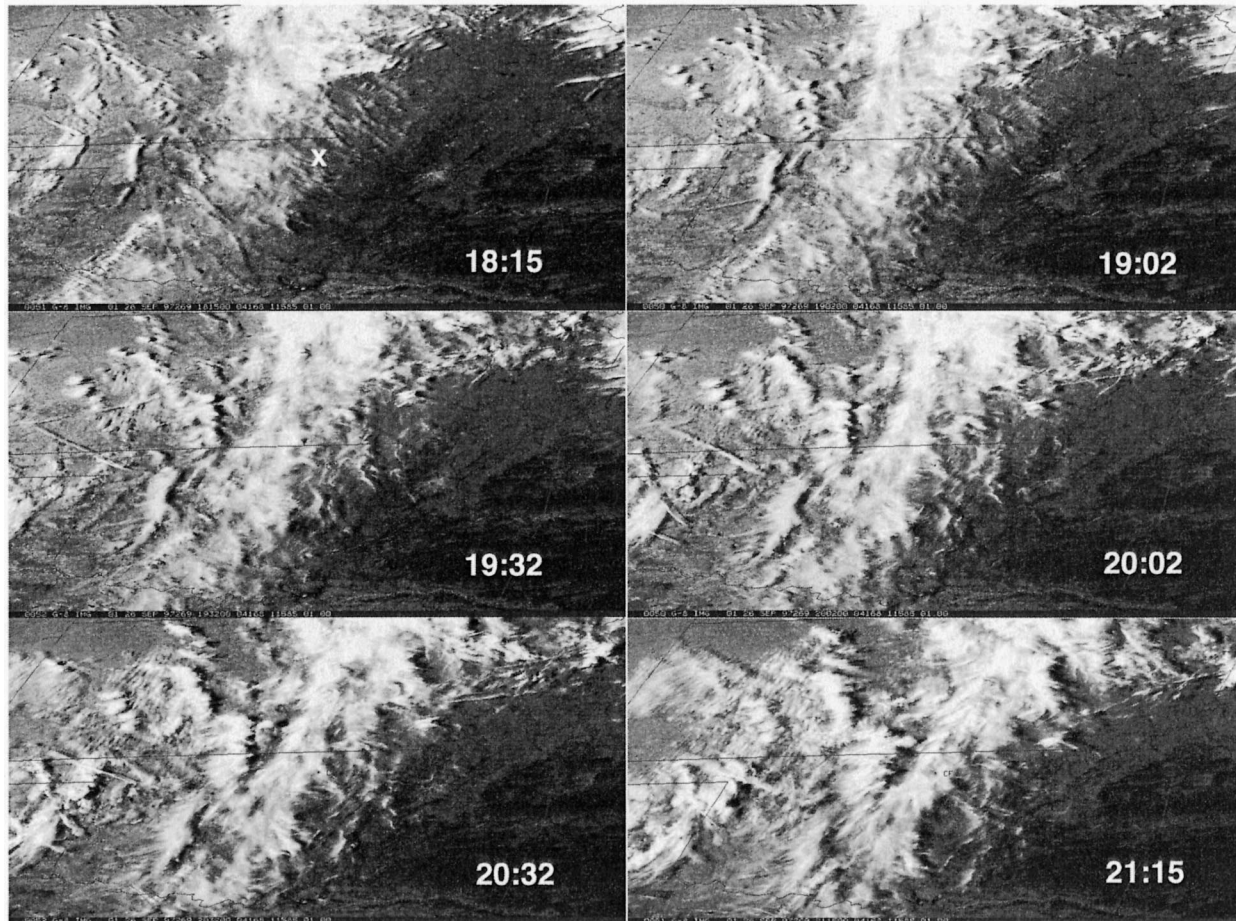


FIG. 4. Expanded views of GOES infrared images over the SGP CART site (X, top left) from 1815 to 2115 UTC on 26 Sep 1997.

vation period on 25 September 1997. During this time, the leading edge of the hurricane cirrus cloud shield moved rapidly over the FARS site from the south (Fig. 2). Shown at top are fish-eye photographs of cloud conditions taken at the indicated times. CPL height versus time displays are given below in terms of relative returned parallel-polarized laser power (based on a logarithmic grayscale), with the local 0000 UTC 26 September temperature (solid line) and dewpoint profiles at right, and linear depolarization ratios (see color  $\delta$  scale at right). Beginning with broken cirrus fibratus coverage, the cirrus layer can be seen to gradually thicken and become dense enough by  $\sim 2000$  UTC to have transformed into altostratus. (Note the loss of sharpness of the solar disk in the 2030 UTC fisheye at upper right, and the attenuated lidar signals.) Originally about 2 km thick, the layer developed several deep particle fall-streaks with tops up to  $\sim 11.5$  km MSL. This active precipitation produced a gradually descending cloud base until  $\sim 1900$  UTC, when the 6.5-km base reached a relatively dry subcloud layer. At this time, particle evaporation promoted 0.5–0.7-km-deep cirrus mammatus structures (Sassen 2002a) below cloud base. This

cloud sequence agrees with the satellite imagery, which shows the cirrus shield leading edge advecting rapidly over FARS on the afternoon of 25 September.

The lidar  $\delta$ -value display at the bottom of Fig. 5 suggests a wide range of cloud microphysical conditions, judging from the near-zero to the maximum  $\sim 0.5$  spread of values. The central part of the layer displays  $\delta \approx 0.2$ , which are somewhat lower than usual for midlatitude cirrus in the  $-20^\circ$  to  $-25^\circ\text{C}$  temperature range (Sassen and Benson 2001), but consistent with those values for cirrus that produce halos (Sassen et al. 2003). On the other hand, the extended regions displaying  $\delta < 0.05$  indicate the presence of horizontally aligned planar ice crystals, as was confirmed by occasionally tipping the lidar a few degrees off the zenith direction. Note how the lowest  $\delta$  values correspond to the strongest lidar backscatter, particularly in the lower cloud during the cirrostratus-to-altostratus cloud transition. Also note that depolarization abruptly increases in the cloud-base region, presumably due to the effects of particle evaporation (i.e., producing crystal sizes too small to orient) and/or aggregation in the mammatus regions.

An unusual (i.e., for FARS) variety of halo and arc

25 September 1997

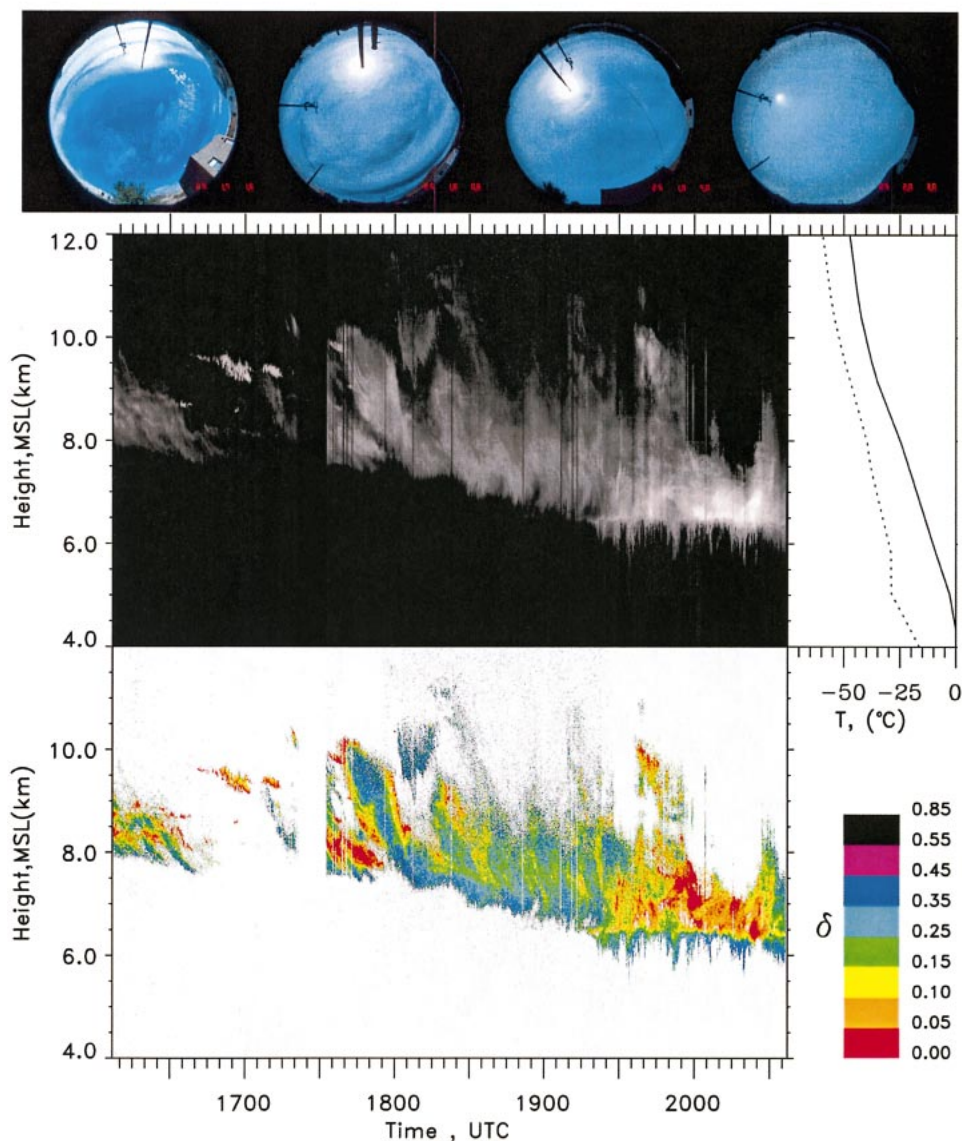


FIG. 5. Summary of remote sensing data collected as the leading edge of the Nora cirrus cloud shield advected over FARS. (top to bottom) Representative fish-eye photographs (note time stamps beginning at 1716 UTC 25 Sep), CPL relative returned energy (based on a logarithmic grayscale), with 0000 UTC Salt Lake City sounding profiles of temperature (solid) and dewpoint temperature at right, and linear depolarization ratio (see color  $\delta$  value key) height vs time displays.

features was observed, although their types and intensities varied over time. The middle fisheyes in Fig. 5 indicate the presence of the  $22^\circ$  halo, upper tangent arc, and segments of the parhelic circle (see also Sassen 1999). Also observed were  $22^\circ$  and  $120^\circ$  parhelia, and a vague upper Parry arc. It is interesting to note that the most brilliant optical displays were observed at about 1800 UTC and from 1930–2000 UTC, times that correspond to the most abundant  $\delta < 0.05$  values in the cirrus before the altostratus advected overhead. Such optically dense ice clouds weaken or destroy optical

displays as seen from the ground because of photon multiple scattering (Tränkle and Greenler 1987).

## 5. The SGP CART dataset

### a. Overview

In addition to the lidar measurements by the PDL at the CART site, the available radar and aircraft data make this a particularly comprehensive cirrus case study. The local Geostationary Operational Environmental Satellite



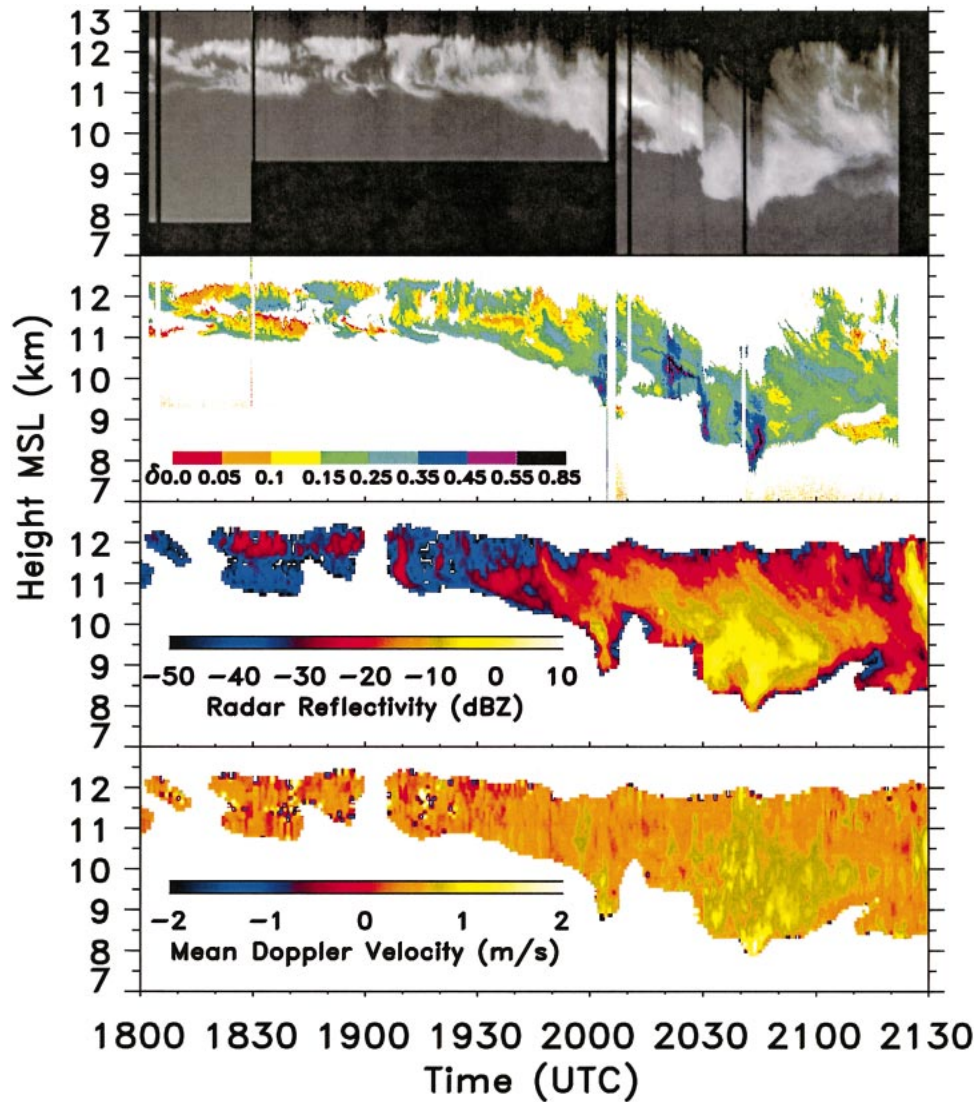


FIG. 6. (top to bottom) Overview of PDL 0.532- $\mu\text{m}$  relative returned energy (based on a logarithmic grayscale) and linear depolarization ratios (see color  $\delta$  value key), and MMCR equivalent radar reflectivity factor and Doppler vertical velocity (see color keys) displays of the cirrus remnants of Nora over the SGP CART site during the Citation aircraft mission on 26 Sep. Positive Doppler velocities indicate downward motions.

(GOES) infrared satellite imagery in Fig. 4 show the movement of the cirrus over the site over the 1800–2130 UTC period of supporting aircraft operations. It can be seen that as the main approximately north–south cirrus cloud band approached from the northwest, a number of small wavelike cirrus structures advected over the CART site until the dense streak arrived at  $\sim 2045$  UTC. According to Fig. 2, this cirrus represented the initial tongue of the hurricane-derived cirrus that was entrained into midlatitude circulations and redirected southward.

A comparison of lidar-attenuated backscattering and depolarization (at 0.532  $\mu\text{m}$ ) with MMCR radar reflectivities and Doppler velocities is provided in Fig. 6.

These data reveal a gradually thickening cirrus layer, which appears to have been optically thick enough to be classified as altostratus at  $\sim 2045$  UTC, although the limited dynamic range of the PDL detectors may have been responsible for the loss of signals near cloud top at that time. The PDL and MMCR have produced unusually similar images of the cloud system, although the radar usually underpredicts cloud-top heights by a few hundred meters, and misses some of the thinnest cirrus at the beginning of the period. In agreement with the satellite images in Fig. 4, the cirrus initially consisted of separated mesoscale uncinus cirrus (MUC) generating regions (Sassen 2002a), until  $\sim 1920$  UTC when the more continuous and vertically developed cir-

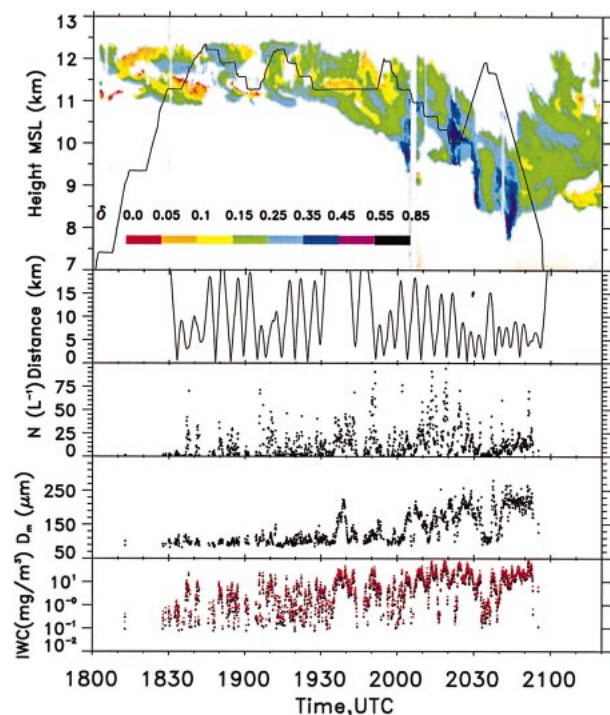


FIG. 7. (top to bottom) Overview of Citation aircraft data in terms of pressure-corrected flight altitude (superimposed over the PDL  $\delta$ -value display), aircraft distance from the CART site, and 5-s averages of 2D-C probe ice crystal number concentration ( $N$ ), average maximum dimension ( $D_{\max}$ ), and IWC derived from the two methods described in the text.

rus moved overhead. Doppler radar velocities (Fig. 6) show evidence for upward motions (red to purple colors) near the heads of the MUCs, followed by precipitation particle-dominated downward motions, sometimes in excess of  $1 \text{ m s}^{-1}$ , in the deep fallstreak patterns embedded in the main cirrus cloud.

As in the case at FARS, both widespread regions of low  $\delta$  values and an unusual variety of cirrus cloud optical displays were observed. The  $\delta < 0.1$  are usually found at the tops of the cirrus generating regions, and generally correspond to the periods when the optical displays were most pronounced. Large areas display  $\delta \approx 0.15$ , while the highest depolarizations (up to  $\sim 0.5$ ) were noted near the bottoms of the dense fallstreaks after 2000 UTC, where the strongest  $Z_e$  indicative of ice crystal aggregates were observed. (Linear depolarization can be expected to increase in aggregates because of the increased shape complexity and the collection of oriented crystals that would otherwise generate specular reflections.) A brilliant  $22^\circ$  halo, tangent arcs, parhelia, and parhelic circle were variably reported by ground observers and the Citation crew. The most brilliant and varied optical displays occurred from  $\sim 1930$ – $2000$  UTC, when large regions of  $\delta < 0.15$  were present. These similarities with the FARS observations, despite the extended ( $\sim 30$  h) period of cloud advection between the two sites, are notable.

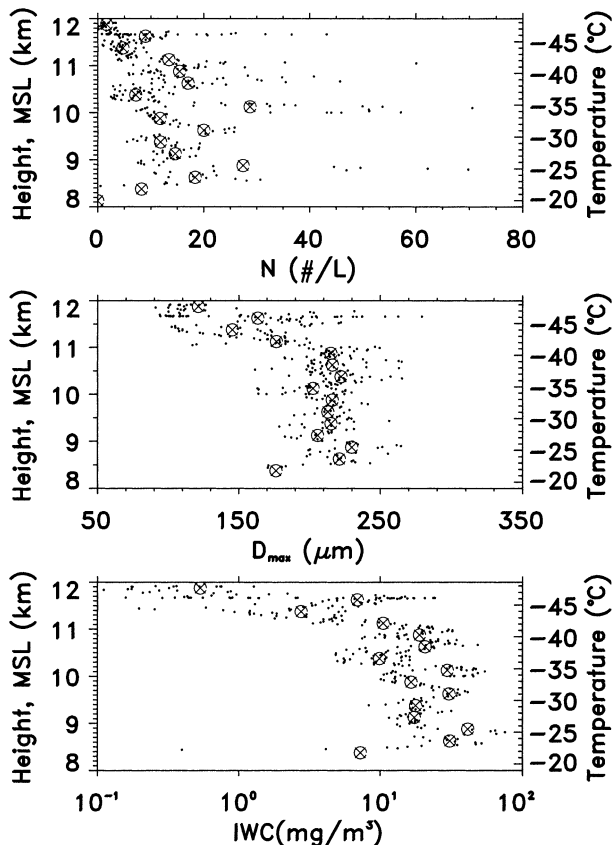


FIG. 8. Vertical profiles of 2D-C measured (top)  $N$ , (middle)  $D_m$ , and (bottom) IWC obtained from 2025 to 2055 UTC on 26 Sep as the Citation performed spirals in the vicinity of the CART site. The  $\otimes$  symbols provide 250-m height averages of the data. Average in situ temperatures are shown at right.

In Fig. 7 we add to this evaluation the in situ data from the Citation. From top to bottom are shown the aircraft flight track, the radial distance of the aircraft from the CART site, and an analysis of 5-s averages of (2D-C probe detected) ice particle concentration  $N$ , mean diameter  $D_m$  (based on the image maximum dimension), and ice water content (IWC). The Citation altitude track has been superimposed on the lidar  $\delta$  value display because it is these remote sensing data that best convey information on ice particle properties for comparison to the in situ findings. The IWC values have been derived through two approaches using the 2D-C probe data. The first is described in Wang and Sassen (2002; see section 6) and the second (red dots) is a more standard approach based on the National Center for Atmospheric Research (NCAR) analysis scheme used at UND. Note that the two methods generally agree to within better than a factor of 2.

There is a tendency for both  $D_m$  and IWC to increase with decreasing height, or increasing temperature, which is better shown in Fig. 8. In view of the cirrus coverage variability over the CART site during the initial broken-cirrus period, it is more appropriate to ex-



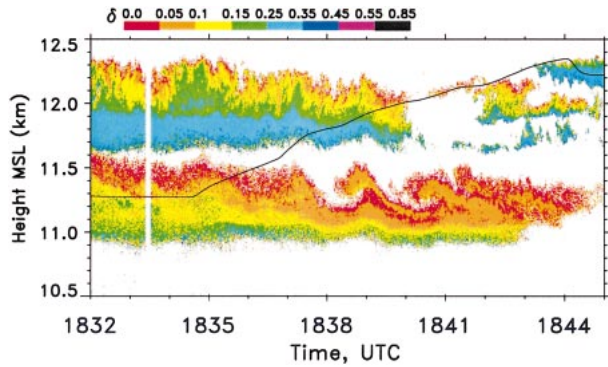


FIG. 9. Expanded view of lidar depolarization from the indicated period, showing a doubled-layered cirrus with breaking K–H waves. Citation aircraft altitude is shown by the superimposed line.

amine the data collected during the final aircraft spiral ascent and descent from 2025–2055 UTC, when the cirrus was more widespread. The vertical profiles of  $N$ ,  $D_m$ , and IWC in Fig. 8 combine the data from the spirals, and 250-m vertical averages of these data quantities are also given. It is clear that, with the exception of the upper cirrus cloud-generating region, most of the cirrus have average  $N \approx 10\text{--}30\text{ L}^{-1}$ ,  $D_m \approx 225\text{ }\mu\text{m}$ , and IWC  $\approx 10\text{--}30\text{ mg m}^{-3}$ . The upper kilometer of cirrus, however, has lower IWC and smaller crystals, which may be responsible for the lower  $N$  because the minimum size threshold ( $D_m = 50\text{--}100\text{ }\mu\text{m}$ ) of the 2D-C probe was approached in this region. The IWC profile displays strong gradients near cloud top and cloud base from crystal nucleation and evaporation, respectively, and a gradual increase within the layer. These average temperature dependencies reflect the effects of the ice crystal growth and sedimentation rates on cirrus cloud formation and maintenance.

#### b. Expanded lidar displays and replicator images

Described here are high-resolution PDL displays and replicator data obtained prior to 1912 UTC, when the in situ device failed. The first example (Fig. 9) from 1832–1845 UTC provides a view of a double-layered cirrus that contains breaking Kelvin–Helmholtz (K–H) waves. The low lidar  $\delta$  values show the presence of horizontally oriented planar ice crystals along the tops of both cloud layers. The small-scale irregularities at the top of the upper layer indicate the presence of numerous cirrus uncinus cell heads. The depolarization in the series of breaking K–H waves is particularly striking, and can be used perhaps to trace the air motions. Figure 10 shows a still higher resolution view of the best-developed K–H wave in terms of relative backscattering and depolarization. It appears that the ice crystals in the breaking wave crest have been drawn up and slid over the previous cloud top, because the lowest  $\delta < 0.05$  are found on the tops of both of these features. It is also interesting to find relatively higher  $\delta$  values,

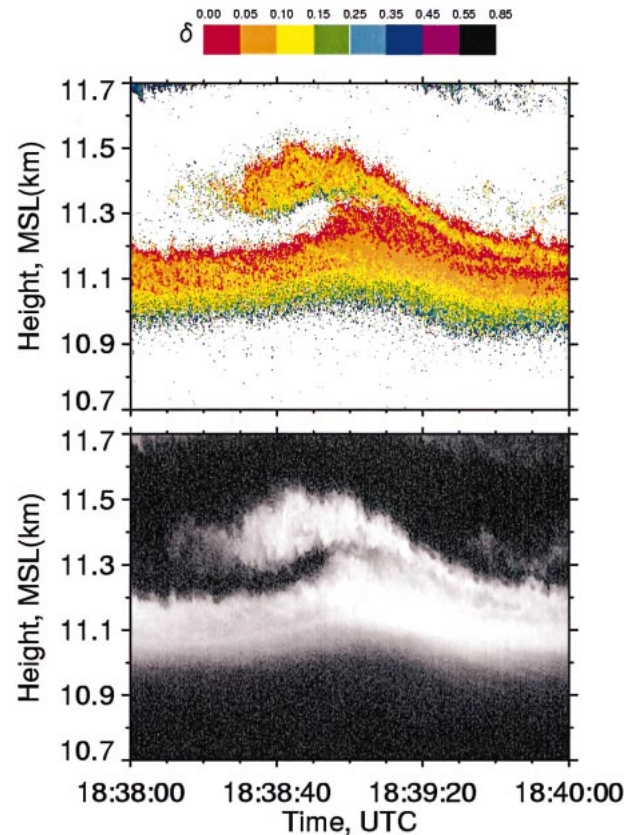


FIG. 10. Detailed view of (top) lidar relative returned energy and (bottom) depolarization in the breaking K–H waves. The lidar data were collected at 1.5-m height and 0.1-s time resolutions.

up to  $\sim 0.25$ , on the underside of the wave crest. This increase in depolarization could be due to particle evaporation effects (from dry air mixing) that made the particles too small to orient at this part of the breaking wave, or perhaps to the aerodynamic disorientation of the crystals from turbulence.

Interestingly, although there is no dramatic wind feature in the 1800 UTC sounding at the level of the K–H waves (Fig. 3), there is an indication of a weak directional shear boundary near 11.0 km with a speed shear of  $\sim 1\text{ m s}^{-1}\text{ km}^{-1}$ . However, small-scale wind features can be highly smoothed during standard operational sonde processing (via Vaisala loran winds). There is also some indication of a thin layer of enhanced static stability at about this height (i.e., a lapse rate minima of  $6.8^\circ\text{C km}^{-1}$  versus values exceeding  $8^\circ\text{C km}^{-1}$  at 0.5 km above and below).

Unfortunately, because of the cirrus spatial variability encountered by the aircraft at this time, the in situ data (Fig. 7) do not closely reflect the local cloud structure observed by the lidar, and the Kelvin–Helmholtz waves were not sampled. Figure 11 provides a montage of selected photomicrographs of ice crystal replicas for two cloud regions. The first corresponds to the penetration of the base of the upper cirrus layer. The initial crystals

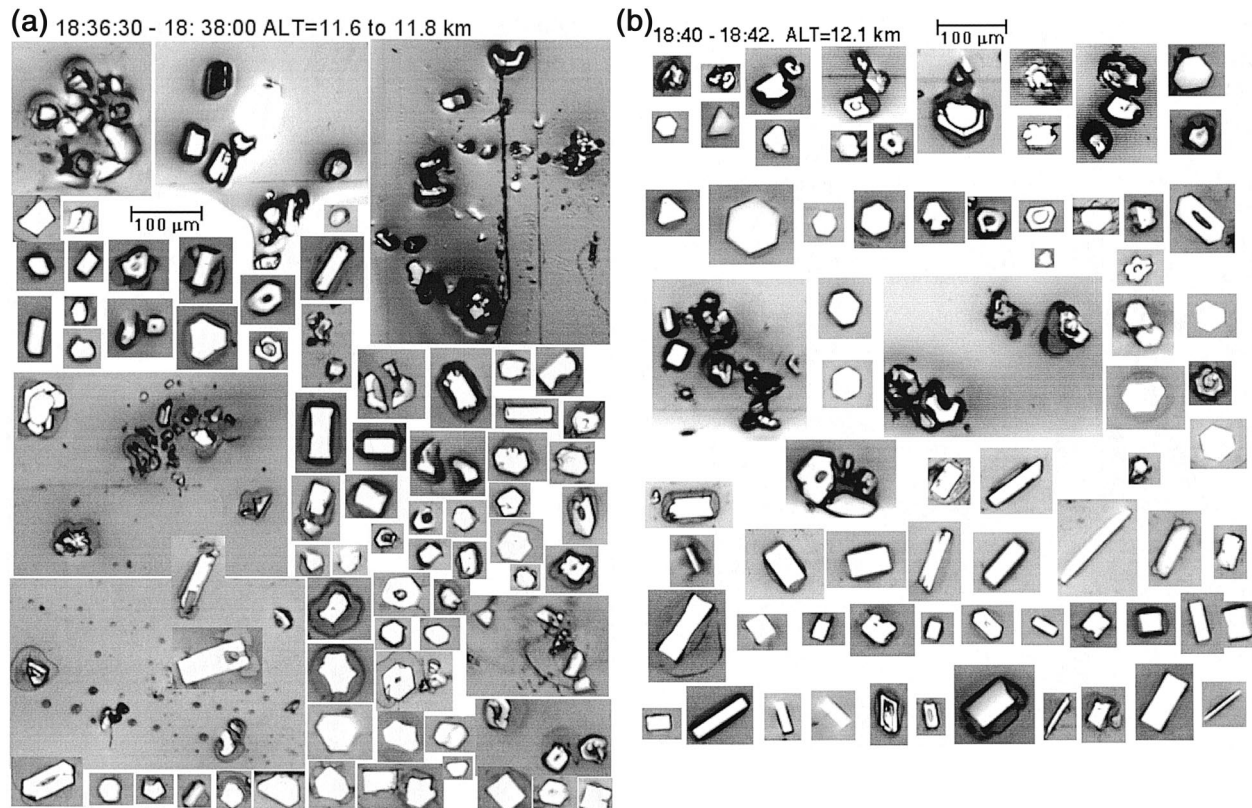


FIG. 11. Sequence of replicator-preserved ice crystal images collected over two periods—(a) 18:36:30–18:38 and (b) 18:40–18:42—corresponding to the aircraft segment in Fig. 9. Note the 100- $\mu\text{m}$  scales near the top.

(top of Fig. 11a) resemble polycrystals or aggregates, which broke apart upon impaction on the substrate, and single crystals that appear to have rounded crystal forms due to sublimation. Most of the remaining crystals are solid plates and columns with maximum dimensions of 25–75  $\mu\text{m}$ . During the second sample (Fig. 11b) the aircraft was at a height corresponding to the top of the upper cirrus layer. These images also reveal mostly solid, pristine ice crystals spanning the habit range from thin plates to long columns, although their sizes some-

times exceed 100  $\mu\text{m}$ . Note that just as the columns display a variety of aspect ratios, it is likely that the planar crystals were also of variable thickness. This indicates that the cirrus composition was generally well mixed due to the effects of vertical motions, particle sedimentation, and turbulent mixing. There are fewer radial polycrystals or aggregates. The 2D-C data (Fig. 7) from both regions show  $D_m$  of  $\sim 100 \mu\text{m}$ , with  $N$  and IWC varying from about 5–75  $\text{L}^{-1}$  and 1–10  $\text{mg m}^{-3}$ , respectively.

The data in Figs. 12–13 show the results of sampling the mesoscale generating region from 1845–1905 UTC. This classic MUC displays a convective-appearing cloud top, a central body of numerous collected fallstreaks, and a tail of virga that has accumulated in an apparently moist layer at the same height as the bottom layer noted just before. Note that the sheared fallstreak patterns at  $\sim 11.5 \text{ km}$  suggest a more structured wind profile than indicated by the soundings (Fig. 3), which could help explain the presence of the breaking K–H waves in Figs. 9 and 10. Lidar  $\delta$  values are again low from oriented ice plates along portions of the tops of the upper and lower clouds, although much of the central body shows  $\delta \approx 0.3$ . Microphysically,  $D_m$  of  $\sim 100 \mu\text{m}$  and a strong variability in  $N$  and IWC are again found in the 2D-C data of Fig. 7. The ice crystal casts in Fig.

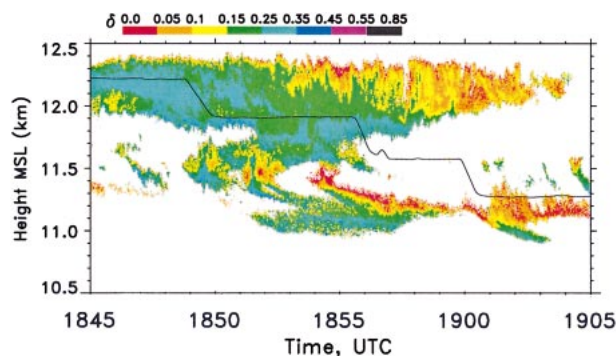


FIG. 12. Expanded view of lidar depolarization, as in Fig. 9, from the indicated period as the aircraft traversed a mesoscale uncinus complex.



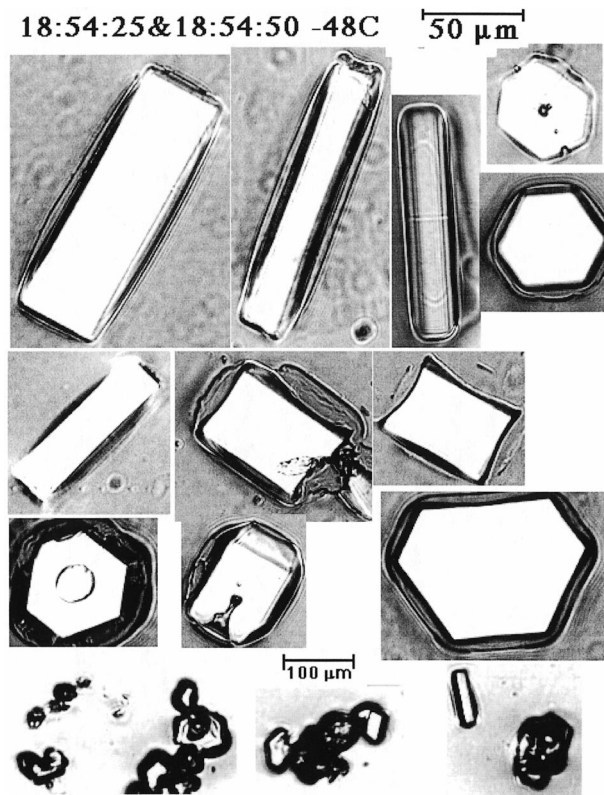


FIG. 13. Sequence of replicator-preserved ice crystal images collected over the period corresponding to a portion of the aircraft segment in Fig. 12.

13 were obtained when the aircraft was nearly overhead, and depict mostly solid pristine plates and columns with 50–150- $\mu\text{m}$  maximum dimensions. Although many of the plates display near-perfect hexagonal perimeters, the 75- $\mu\text{m}$  plate at lower right is clearly an uneven hexagon. Note also the long column with rounded ends and linear and elliptical surface designs, and the evidence for shattered radial crystals at bottom. Finally, as discussed below, some of the particles have central features ranging in diameter from  $\sim 5$  to 20  $\mu\text{m}$ .

The final example in Fig. 14 from 1905–1920 UTC depicts the last recognizable MUC before the cirrus layer became continuous and began a sudden deepening. Its structure is similar to that described above, but smaller regions display the low  $\delta$  values indicative of oriented plates. The 2D-C on the Citation measured somewhat higher  $D_m$ ,  $N$ , and IWC (Fig. 7) as it ascended through the body of the MUC, indicating more active ice particle generation and growth. Radar reflectivities have also increased and Doppler velocities show relatively stronger updrafts in the central fallstreak (Fig. 6).

The replicator images in Fig. 15 are broken into four intervals as the Citation ascended in a spiral from 11.4 to 12.2 km ( $-43^\circ$  to  $-49^\circ\text{C}$ ). In the initial sample (Fig. 15a) from the 11.4-km height that earlier displayed oriented plate crystals, a number of plates  $>100 \mu\text{m}$  in

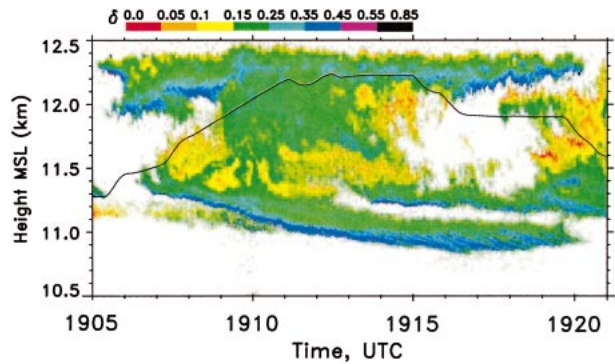


FIG. 14. Expanded view of lidar depolarization, as in Fig. 12.

diameter are present, along with whole and broken mostly solid columns and platelike polycrystals. Almost all of the plates display either threefold trigonal symmetry or uneven hexagonal shapes: whether such shapes are more or less likely to maintain stable orientations is unclear. Figure 15b shows a large aggregate and stout columns, but fewer large plates. Note the shattered  $\sim 100 \mu\text{m}$  plate at bottom right, the bulletlike crystal to the left of the 50- $\mu\text{m}$  scale, and the column above with a central elliptical design. Continuing upward, the next sample (Fig. 15c) contains mainly smaller plates, some of which appear to be poorly preserved, and others that have grossly distorted hexagonal perimeters (e.g., top left). The largest plate at center left has been broken on impact, and to the right is a column with tapered ends that resembles a pyramidal crystal. The final sample, from a height near cloud top with the highest  $\delta$  values, is dominated by long mostly solid columns and apparent plate polycrystals. Some plates with trigonal and hexagonal symmetries are present, but are generally  $<100 \mu\text{m}$ . The crystal at bottom left has a fourfold perimeter and an odd internal design, suggesting cubic symmetry. In general, fragmented radial crystals are now more common in this MUC, which can help explain the higher  $\delta$  values, radar reflectivity, and Doppler velocities measured at this time.

As mentioned above, some of the plates and columns display an unusual feature: a central circular or irregular design. Figure 16 shows a group of these particles, which we suggest contain marine microbes that acted as ice nuclei. We acknowledge that the central markings on many crystals could represent circular growth terraces (or pits) on the crystal faces that were preserved in the particle casts: this particle morphology is not uncommon (see e.g., Sassen and Takano 2000). However, the resemblance of some of the central features to cellular morphology is so strong that biogenic ice nuclei are indicated. Many of the smaller central “dots” have no recognizable features, but are located precisely at the particle center, where ice nuclei are to be expected. Note that any internal central cavity will not be preserved in the replicas, and the film depth is typically too thin to allow the preservation of the upper crystal face. Thus,

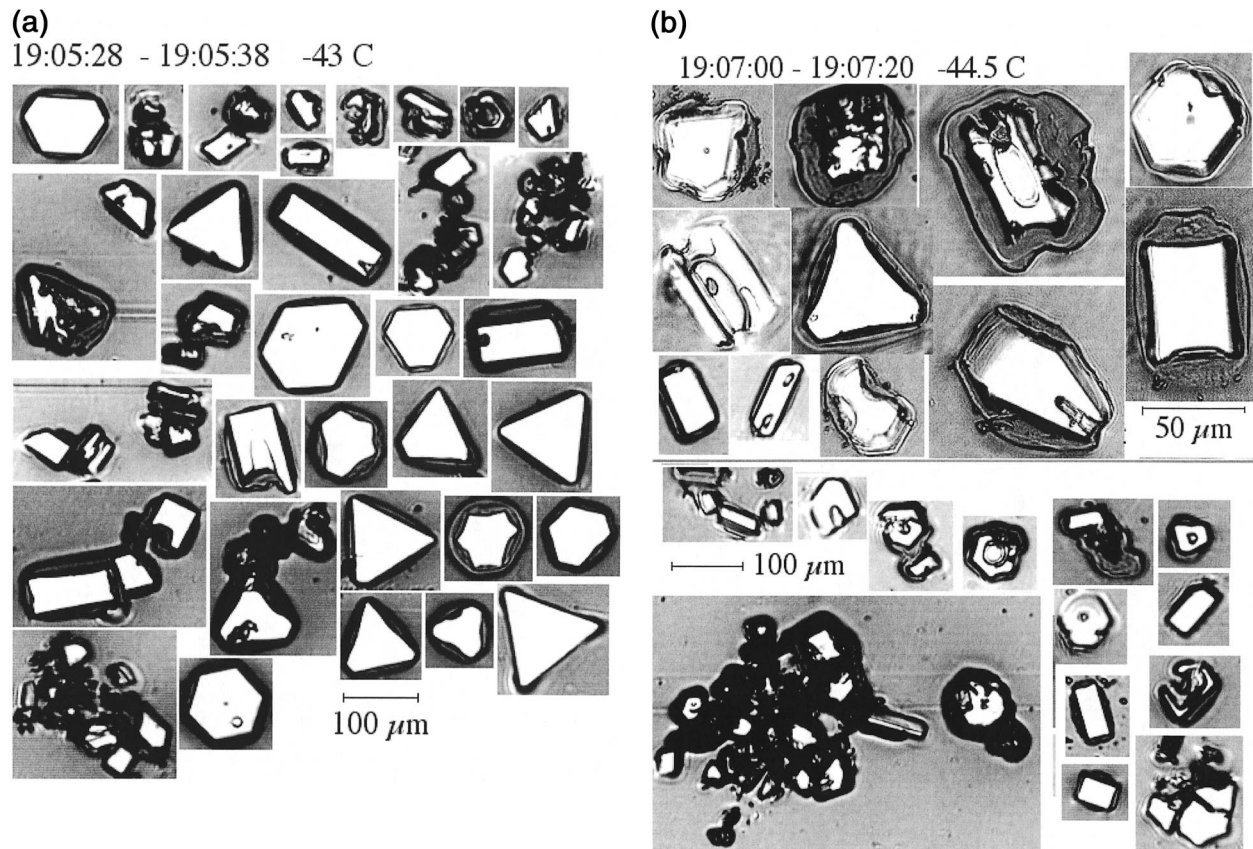


FIG. 15. Sequence of replicator-preserved ice crystal images collected over four sampling periods within the aircraft segment shown in Fig. 14. While (a) and (c) depict one particle scale each, in (b) and (d) two size scales separated by horizontal lines have been used in the images.

we are normally left with a hollow depression in the film after the sublimation of the ice, and any insoluble materials are deposited on the bottom of the particle cast.

### c. Microphysical inferences

Examination of the lidar depolarization data reveal that  $\delta$  ranges from  $\sim 0$  to 0.4, which reflects various ice crystal shapes and orientations that are not unusual for cirrus (Sassen and Benson 2001), particularly those generating halos (Sassen et al. 2003). The near-zero  $\delta$  are caused by a laser backscattering medium dominated by horizontally oriented plate crystals, and the influence of this anisotropy diminished over the period that the cirrus cloud system developed. These regions are typically found at and near the tops of the cloud layers, whereas the strongest depolarization occurs near the cloud bases. The planar crystals often appear to be generated in cloud-top uncinus cells and are able to maintain their orientations in fallstreaks up to  $\sim 0.5$  km in depth. Thus, the usual gradient in  $\delta$  values observed from cirrus layer top to base must reflect basic thermodynamical conditions favorable for the growth of large plates, including

temperature and water vapor supersaturation. It is probable that plate crystal growth is favored by the relatively high supersaturations that are required for ice nucleation at cloud tops, although also important is the concentration of nucleated crystals competing for the available moisture supply, which is influenced by the updraft velocity (Lin et al. 2002). The transformation of plates into thick plates and columns occurs in different environments encountered during particle sedimentation. Finally, the highest depolarization measured near cloud bases (see especially Fig. 14) may reflect the effects of particle aggregation, or alternatively, crystal evaporation, which made the plates too small to orient aerodynamically.

Although the position of the aircraft rarely corresponded closely to the lidar zenith sample volume, the general types of ice crystals replicated can be compared to the lidar depolarization data. The preserved crystal shapes show that a wide range of ice crystal aspect ratios, from thin plates to long columns, and radial crystals or aggregates, were indeed sampled in situ. As for the plate crystals, the ability to uniformly orient in space stems from the action of aerodynamic drag forces, which are functions of particle fall speed (i.e., shape, density,



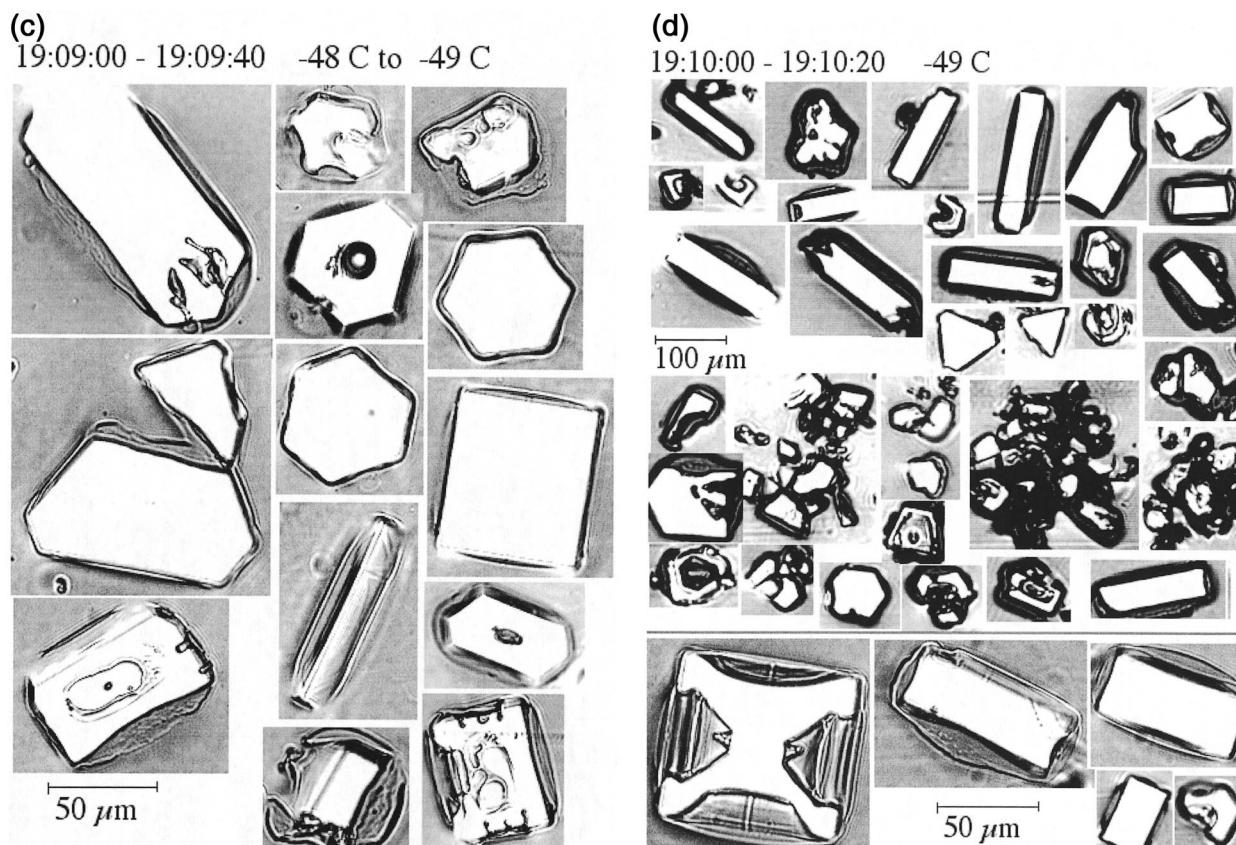


FIG. 15. (Continued)

and size) and air density (height). The Reynolds number  $Re = vd/\nu$  provides a convenient factor to relate the particle terminal velocity  $v$ , diameter  $d$ , and kinematic viscosity  $\nu$  of the fluid proportional to air pressure. (For ice crystals falling in air,  $d$  is usually taken as the particle maximum dimension.) A variety of evidence indicates that stable particle fall attitudes are achieved under the condition  $1 < Re < 100$ . According to current knowledge,  $Re = 1$  corresponds to  $d \approx 200\text{--}300\ \mu\text{m}$  for plate and thick plate crystals at a typical cirrus cloud pressure of 300 mb (Sassen 1980).

However, it is apparent from Figs. 11, 13, and 15 that few planar ice crystals much larger than  $\sim 100\ \mu\text{m}$  were preserved. [Columnar crystals  $> 200\ \mu\text{m}$  that are certainly large enough to orient horizontally are present, but a Parry arc would have been the signature of columns oriented with prism faces parallel to the ground (Sassen and Takano 2000).] On the other hand, the maximum 2D-C image diameters (not shown) during this period are often  $200\text{--}300\ \mu\text{m}$ , which are (marginally) in line with the earlier research based on light pillar observations (Sassen 1980). Thus the fracturing of large planar ice crystals during impaction on the replicator substrate may have affected the results, as can often be seen in the shattered plates of  $\sim 100\ \mu\text{m}$  diameter (see, e.g., Fig. 15c). Moreover, as shown by Sassen and Ben-

son (2001), only a relatively few plates need be horizontally oriented in order to significantly reduce zenith lidar  $\delta$  values; for example, about 1 properly oriented plate out of 100 would generate  $\delta \sim 0.05$ . Nonetheless, the in situ evidence suggests that ice crystals somewhat smaller than previously thought may maintain near-horizontal orientations. This may be particularly true in the Hurricane Nora cirrus case, because the fall patterns of the regular solid crystal shapes could be unusually stable. Also, the visualization of nocturnal light pillars may require very small crystal departures from the horizontal plane relative to zenith lidar measurements. Thus we conclude that planar ice crystals on the order of  $100\text{--}200\text{-}\mu\text{m}$  diameter at cirrus altitudes are probably sufficiently large to develop fall attitudes stable enough to be identified by polarization lidar.

## 6. Retrieved microphysical and radiative properties

Improving multiple remote sensor algorithms for the estimation of cirrus cloud microphysical and radiative properties hold promise for more accurately characterizing these important cloud quantities from the ground. Here, in order to provide much more continuous vertical information than is possible from aircraft operations, we

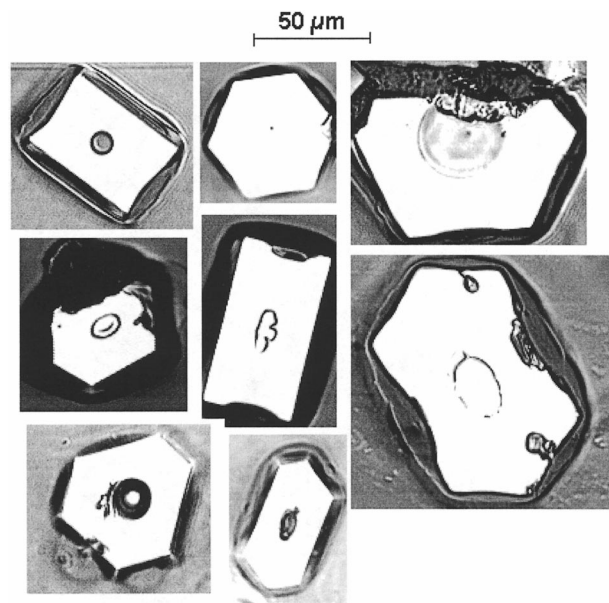


FIG. 16. Selected replicator images of plate and column ice crystals showing central features resembling plankton and other microbes ranging from a few microns up to  $\sim 40 \mu\text{m}$  in maximum dimension. Note the apparent algae cell at the center of the broken plate crystal (top right), which displays features of cell morphology.

have taken advantage of these recent developments to convert the remote sensing data into fields of general effective size  $D_{\text{ge}}$  and IWC (see Fu 1996), and the vertically integrated quantities of ice water path (IWP), infrared layer emittance  $\epsilon$ , and visible cloud optical depth  $\tau$ .

The method used for deriving  $D_{\text{ge}}$ , IWC, and IWP in Fig. 17 relies on the combined analysis of the MMCR  $Z_e$  and Raman lidar visible extinction coefficient  $\sigma$  (per kilometer), as described in Wang and Sassen (2002). It is based on the treatment of cirrus cloud radiative properties developed by Fu (1996), in which  $\sigma$  is parameterized as functions of IWC,  $D_{\text{ge}}$ , and two constants at the lidar wavelength. Using the same assumptions regarding ice crystal shape as in Fu (1996), and further assuming that the Rayleigh approximation is valid and the radar reflectivity of hexagonal ice crystals is equal to that of an equivalent volume ice sphere,  $Z_e$  can be parameterized approximately as  $Z_e = C'(IWC/\rho_i) D_{\text{ge}}^b$ , where  $C'$  and  $b$  are constants based on a modified gamma size distribution and  $\rho_i$  is the density of ice. Note that the algorithm results have been tested against the aircraft data obtained in this case study (Wang and Sassen 2002) and good agreement was found for spatially consistent data. To derive the (red)  $\tau$  and  $\epsilon$  traces in Fig. 17, we have used the combined lidar and infrared radiometer (LIRAD) approach, using PDL backscatter and coaligned midinfrared radiometer data (Comstock and Sassen 2001). The comparison of LIRAD-derived  $\tau$  with that provided by the direct analysis of the Raman lidar data shows quite good agreement.

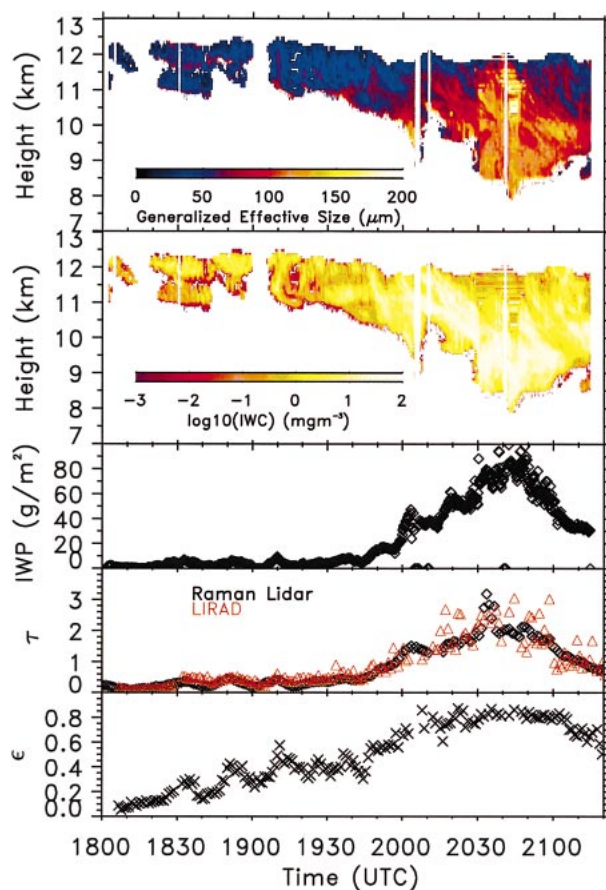


FIG. 17. Composite of data derived from SGP CART data using an advanced radar/lidar algorithm that infers, from top to bottom, generalized effective size field, field of log IWC, vertically integrated IWP, visible cloud optical depth ( $\tau$ , using the two methods described in the text), and infrared layer emittance ( $\epsilon$ ) over the period of the aircraft mission.

The results in Fig. 17 are in compliance with expectations for midlatitude cirrus (see Sassen 2002a). The initial  $\sim 1.5$  km deep cirrus fibratus can be seen to be composed of relatively small ( $< \sim 50 \mu\text{m}$ ) effective particle sizes that produce correspondingly small IWP values, except in the central fallstreak of the final MUC at 1910 UTC. The mostly  $\tau < \sim 0.3$  and  $\epsilon < 0.4$  before this time are consistent with thin (i.e., bluish-appearing) cirrus. All derived data quantities increase with vertical cloud development, and then decrease after the peak cloud depth is attained. In particular,  $D_{\text{ge}}$  and IWC increase in the upper cloud region, indicating conditions more favorable for active particle growth. Note also how the  $\tau \approx 3.0$  and  $\epsilon \approx 0.85$  limits for cirrostratus (Sassen 2002a) are approached when the cirrus reaches its maximum depth at  $\sim 2045$  UTC.

## 7. Discussion and conclusions

This cirrus cloud case study is rare both because of the comprehensive resources that were used to observe



it from two major remote sensing facilities in the western and central United States, and the nature of the cirrus itself: midlatitude cirrus that evolved over a period of days out of hurricane outflow. The convectively derived tropical cirrus soon became maintained by extratropical processes as it advected inland. Simple particle fall speed considerations show that the ice mass generated originally over the eastern Pacific Ocean could not persist for long due to particle fallout. Thus, the only long-lasting impact of the initial generation mechanism must be found in the upper tropospheric reservoir of CCN that was raised from the ocean's surface during strong organized convection. The generation rates of sea salt particles and droplets from the oceans surface are controlled by the surface wind speed (Monahan et al. 1983). In addition to the generation of marine aerosols from breaking waves through the bursting bubble mechanism, at wind speeds  $>9 \text{ m s}^{-1}$  great numbers of spume droplets are created as wave crests are torn apart by wind action. O'Dowd and Smith (1993) reported sea salt CCN concentrations up to  $100 \text{ cm}^{-3}$  at a wind speed of  $20 \text{ m s}^{-1}$ : the particles were characterized by three log-normal size distributions according to the production mechanism, corresponding to number mode radii of 0.1, 1.0, and  $6.0 \text{ }\mu\text{m}$ . Thus, it is indicated that the great surface wind speeds within hurricanes can generate, and loft to high altitudes in convective updrafts, large quantities of both small and large marine particles. In this case, surface wind speeds up to  $\sim 60 \text{ m s}^{-1}$  were associated with Hurricane Nora.

Although giant CCN scavenging through precipitation processes may be an effective sink for many of the lofted marine particles, the remaining CCN, and aerosol recycling after ice particle evaporation, represent a source of future cirrus cloud particles. According to model simulations (Lin et al. 2002), with time, increasingly small CCN would tend to come into play in cirrus formation under these conditions. The presence of apparent marine biogenic ice nuclei with diameters up to  $40 \text{ }\mu\text{m}$  at the centers of ice crystal replicas demonstrates the efficacy of this lofting mechanism following spume droplet production at the ocean's surface.

Although further investigation is planned, these observations for the first time illustrate that marine microbiota can serve as ice nuclei in cirrus clouds. Since the numbers of such identified particles are relatively small, however, this mechanism may be unimportant in this particular case. Previously, Brier and Cline (1959) showed ocean water to be a source of IN and Saxena (1983) found evidence for the presence of biogenic nuclei in Antarctic coastal clouds. The efficacy of both terrestrial and marine microbes in initiating the ice phase in the laboratory has been summarized by Schnell and Vali (1976). The processing of marine boundary layer air by convective clouds has also been shown to generate high concentrations of new aerosol particles in the free troposphere with the aid of photochemistry (Clarke et al. 1998), but such minute particles may not be able to

compete effectively with the background of larger cloud-forming nuclei in cirrus. The model study of Ghan et al. (1998) illustrates how sea salt CCN can successfully compete (in droplet clouds) with background populations of sulfate particles, which in this case may have been introduced through mixing with midlatitude air.

The concept that basic cloud microphysical and radiative properties may be influenced by the cloud generation mechanism is not new, and differences in some properties have already been shown to exist within the FARS midlatitude cirrus cloud dataset (Sassen and Comstock 2001). In that study, midlatitude synoptic, orographic, and anvil cirrus clouds displayed dissimilar properties in terms of their  $\tau$ -versus- $\varepsilon$  relations and backscatter-to-extinction ratios, which can be expected due to the effects of the strengths of typical updrafts, cloud formation temperature, and, importantly, the source of CCN.

We have pointed out here that the Hurricane Nora cirrus cloud shield system contained extensive regions of horizontally oriented pristine, solid ice crystals, which were effective at generating uncommon optical displays. As a matter of fact, the presence of the brilliant halos and arcs can be said to have served as a tracer for the hurricane-derived cirrus during transport. In contrast, midlatitude cirrus clouds appear to be rather poor at generating brilliant optical displays other than the "common"  $22^\circ$  halo because of the typical cirrus ice crystal morphology, which appears to be dominated by hollow and irregular particles (Sassen et al. 1994). According to the analysis of the cirrus cloud optical displays at FARS (Sassen et al. 2003), the optical displays observed on 25 September 1997 were among the most complex and brilliant. Furthermore, there is previous evidence that midlatitude cirrus derived from hurricanes or tropical flow can generate unusual optical displays. Although antidotal, we note that the subhorizon counterpart of the parhelic circle, the subparhelic arc, along with the rare anthelion, were photographed over western New York from an aircraft above the extensive cirrus shield created by the October 1996 Caribbean Hurricane Josephine (see Sassen et al. 1998a). The best optical display studied at FARS occurred in connection with a tropical cirrus cloud system, which produced an exceptional Parry arc (Sassen and Takano 2000).

It should be emphasized that the Nora ice crystals are unique among the data collected by the Desert Research Institute replicator in cirrus clouds for their solid, pristine qualities, occasional rare shapes, and the relative scarcity of polycrystals or aggregates. That this is so can be appreciated by examining the extensive midlatitude cirrus replica data sample compiled online (see <http://www.dri.edu/Projects/replica>). We should also stress that the hurricane-derived cirrus considered here were modified by aging processes and mixing with midlatitude air, and so should not be compared to *fresh* anvil cirrus in the Tropics, which appear to contain very

different ice crystal types (McFarquhar and Heymsfield 1996).

This information leads us to speculate that the aqueous phase chemistry associated with ice nucleation and growth may be of paramount importance to subsequent ice particle morphology. The consequences are significant not only to halo formation, but analogously to the basic manner in which solar radiation is scattered by ice clouds. With the exception of the homogeneous freezing of pure water drops, which in reality does not apply to the upper troposphere, we are confronted with comprehending the growth of ice crystals from variously contaminated aqueous solutions. In the case of the freezing of supercooled *cloud droplets* (i.e., ice nucleation essentially at water saturation, or at  $\sim -38^\circ\text{C}$ ), the contamination from even extremely diluted inorganic salt solutions has a significant impact on ice crystal morphology (Finnegan and Pitter 1997). Studies indicate that such conditions produce liquid or liquidlike layers on the growing ice surfaces, which generate charge separations depending on the nature of the contaminant (Workman and Reynolds 1950). For example, under the same conditions alkali salts confer an opposite charge polarity in the ionic sea salt solution layer as compared to ammonium salt solutions. In contrast, essentially nothing is known of the situation applicable to cirrus ice crystal growth at colder temperatures. It is precisely the impacts of the haze particle freezing process in cold, concentrated solution droplets (in the form of haze particles undergoing the Köhler swelling process) that is of major consequence for improving our comprehension of basic cirrus cloud properties.

Improving this knowledge could lead to the introduction in large-scale models of a geographical and seasonal dependence of cirrus radiative properties, depending on, for example, the influence of oceanic deep convective activity. It may be possible to break down the problem into a limited number of categories that depend on the CCN source and composition. Based on laboratory and recent cirrus research, we can now identify at least the following distinct cirrus cloud ice nucleation and growth processes that are dominated by the following:

- 1) homogeneous freezing of sulfate of ammonia droplets, probably the *normal* mode of midlatitude cirrus ice crystal production (Sassen and Dodd 1988; Heymsfield and Sabin 1989; Tabazadeh and Toon 1998);
- 2) homogeneous freezing of aqueous sulfuric acid droplets in tropopause-topped cirrus, or along tropopause folds, apparently associated with the uncommon cirrus corona display (Sassen et al. 1995, 1998b);
- 3) heterogeneous freezing via biogenic and other IN of solution droplets through the condensation-freezing process (DeMott et al. 1998), but also dependent on the aqueous phase chemistry (Finnegan and Pitter 1997);
- 4) dry or wet deposition on special mineral particles such as desert dusts that have been shown to be effective IN (Isono et al. 1959; Schaller and Fukuta 1979; Sassen 2002b);
- 5) homogeneous freezing of sea salt solution droplets, as suggested here on the basis of unusual halo production (see also Sassen and Takano 2000).

Each of these ice nucleation mechanisms has the potential for affecting cirrus cloud composition through differences in particle shape, and possibly also on the nucleation rate, which controls particle concentration and the subsequent crystal sedimentation rate (Lin et al. 2002). Now that the global nature of cirrus clouds is coming under increased scrutiny, comprehending these nucleation-dependent differences in cirrus cloud microphysical and radiative properties may allow us to improve our radiative parameterizations in improved models for the benefit of climate research.

**Acknowledgments.** This research has been funded by DOE Grants DEFG02ER1059 and DEFG0398ER62571 from the Atmospheric Radiation Measurement program, NSF Grant ATM-0119502, and NASA Grant NAG56458. We thank J. M. Comstock for providing the LIRAD data analysis.

#### REFERENCES

- Arnott, W. P., Y. Y. Dong, and J. Hallet, 1994: Role of small ice crystals in radiative properties of cirrus: A case study, FIRE II, November 22, 1991. *J. Geophys. Res.*, **99**, 1371–1381.
- Brier, G. W., and D. B. Cline, 1959: Ocean water as a source of ice nuclei. *Science*, **130**, 717–718.
- Chen, Y., P. J. DeMott, S. M. Kreidenweis, D. C. Rogers, and D. E. Sherman, 2000: Ice formation by sulfate and sulfuric acid aerosol particles under upper-tropospheric conditions. *J. Atmos. Sci.*, **57**, 3752–3766.
- Clarke, A. D., J. L. Varner, F. Eisle, R. L. Mauldin, D. Turner, and M. Litchy, 1998: Particle production in the remote marine atmosphere: Cloud outflow and subsidence during ACE 1. *J. Geophys. Res.*, **103**, 16 397–16 409.
- Comstock, J. M., and K. Sassen, 2001: Retrieval of cirrus cloud radiative and backscattering properties using combined lidar and infrared radiometer (LIRAD) measurements. *J. Atmos. Oceanic Technol.*, **18**, 1658–1673.
- DeMott, P. J., D. C. Rogers, S. M. Kreidenweis, Y. Chen, C. H. Twohy, D. Baumgardner, A. J. Heymsfield, and K. R. Chan, 1998: The role of heterogeneous freezing nucleation in upper tropospheric clouds: Inferences from SUCCESS. *Geophys. Res. Lett.*, **25**, 1387–1390.
- Duda, D. P., P. Minnis, and L. Nguyen, 2001: Estimates of cloud radiative forcing in contrail clusters using GOES imagery. *J. Geophys. Res.*, **106**, 4927–4937.
- Finnegan, W. G., and R. C. Pitter, 1997: Ion-induced charge separations in growing single ice crystals: Effects on growth and interaction processes. *J. Colloid Interface Sci.*, **189**, 322–327.
- Fu, Q., 1996: An accurate parameterization of the solar radiative properties of cirrus clouds for climate models. *J. Climate*, **9**, 2058–2082.
- Ghan, S. J., G. Guzman, and H. Abdul-Razzak, 1998: Competition between sea salt and sulfate particles as cloud condensation nuclei. *J. Atmos. Sci.*, **55**, 3340–3347.
- Goldsmith, J. E. M., F. H. Blair, S. E. Bisson, and D. D. Turner, 1998:



- Turn-key Raman lidar for profiling atmospheric water vapor, clouds, and aerosols. *Appl. Opt.*, **37**, 4979–4990.
- Heymsfield, A. J., and R. M. Sabin, 1989: Cirrus crystal nucleation by homogeneous freezing of solution droplets. *J. Atmos. Sci.*, **46**, 2252–2264.
- Isono, K., M. Komabayashi, and A. Ono, 1959: The nature and origin of ice nuclei in the atmosphere. *J. Meteor. Soc. Japan*, **37**, 211–233.
- Kalnay, E., and Coauthors, 1996: The NCEP/NCAR 40-Year Reanalysis Project. *Bull. Amer. Meteor. Soc.*, **77**, 437–471.
- Lin, R. F., D. O'C. Starr, P. J. DeMott, R. Cotton, K. Sassen, E. Jensen, B. Karcher, and X. Jiu, 2002: Cirrus parcel model comparison project. Phase 1: The critical components to simulate cirrus initiation explicitly. *J. Atmos. Sci.*, **59**, 2305–2329.
- McFarquhar, G. M., and A. J. Heymsfield, 1996: Microphysical characteristics of three anvils sampled during the Central Equatorial Pacific Experiment. *J. Atmos. Sci.*, **53**, 2401–2423.
- Monahan, E. C., C. W. Fairall, K. L. Davidson, and P. J. Boyle, 1983: Observed inter-relations between 10 m winds, ocean whitecaps and marine aerosols. *Quart. J. Roy. Meteor. Soc.*, **109**, 379–392.
- Moran, K. P., B. E. Martner, M. J. Post, R. A. Kropfli, D. C. Welsh, and K. B. Widener, 1998: An unattended cloud-profiling radar for use in climate research. *Bull. Amer. Meteor. Soc.*, **79**, 443–455.
- O'Dowd, C. D., and M. H. Smith, 1993: Physicochemical properties of aerosols over the northeast Atlantic: Evidence for wind speed related submicron sea-salt aerosol production. *J. Geophys. Res.*, **98**, 1137–1149.
- Pruppacher, H. R., and J. D. Klett, 1997: *Microphysics of Clouds and Precipitation*. 2d ed. Kluwer Academic, 954 pp.
- Sassen, K., 1980: Remote sensing of planar ice crystal fall attitudes. *J. Meteor. Soc. Japan*, **58**, 422–429.
- , 1999: Cirrus clouds and haloes: A closer look. *Optics and Photonics News*, Vol. 10, Optical Society of America, 39–42.
- , 2002a: Cirrus clouds: A modern perspective. *Cirrus*, D. Lynch et al., Eds., Oxford University Press, 11–40.
- , 2002b: Indirect climate forcing over the western US from Asian dust storms. *Geophys. Res. Lett.*, **29** (10), 1465, doi:10.1029/2001GL014051.
- , and G. C. Dodd, 1988: Homogeneous nucleation rate for highly supercooled cirrus cloud droplets. *J. Atmos. Sci.*, **45**, 1357–1369.
- , and Y. Takano, 2000: Parry arc: A polarization lidar, ray tracing, and aircraft case study. *Appl. Opt.*, **39**, 6738–6745.
- , and S. Benson, 2001: A midlatitude cirrus cloud climatology from the Facility for Atmospheric Remote Sensing. Part II: Microphysical properties derived from lidar depolarization. *J. Atmos. Sci.*, **58**, 2103–2112.
- , and J. R. Campbell, 2001: A midlatitude cirrus cloud climatology from the Facility for Atmospheric Remote Sensing. Part I: Macrophysical and synoptic properties. *J. Atmos. Sci.*, **58**, 481–496.
- , and J. M. Comstock, 2001: A midlatitude cirrus cloud climatology from the Facility for Atmospheric Remote Sensing. Part III: Radiative properties. *J. Atmos. Sci.*, **58**, 2113–2127.
- , N. C. Knight, Y. Takano, and A. J. Heymsfield, 1994: Effects of ice crystal structure on halo formation: Cirrus cloud experimental and ray-tracing modeling studies. *Appl. Opt.*, **33**, 4590–4601.
- , and Coauthors, 1995: The 5–6 December 1991 FIRE IFO II jet stream cirrus case study: Possible influences of volcanic aerosols. *J. Atmos. Sci.*, **52**, 97–123.
- , W. P. Arnott, J. M. Barnett, and S. Aulenbach, 1998a: Can cirrus clouds produce glories? *Appl. Opt.*, **37**, 1427–1433.
- , G. G. Mace, J. Hallett, and M. R. Poellot, 1998b: Corona-producing ice clouds: A case study of a cold cirrus layer. *Appl. Opt.*, **37**, 1477–1585.
- , J. M. Comstock, Z. Wang, and G. G. Mace, 2001: Cloud and aerosol research capabilities at FARS: The Facility for Atmospheric Remote Sensing. *Bull. Amer. Meteor. Soc.*, **82**, 1119–1138.
- , J. Zhu, and S. Benson, 2003: A midlatitude cirrus cloud climatology from the Facility for Atmospheric Remote Sensing. Part IV: Optical displays. *Appl. Opt.*, **42**, 322–341.
- Saxena, V. K., 1983: Evidence of the biogenic nuclei involvement in Antarctic coastal clouds. *J. Phys. Chem.*, **87**, 4130–4134.
- Schaller, R. C., and N. Fukuta, 1979: Ice nucleation by aerosol particles: Experimental studies using a wedge-shaped ice thermal diffusion chamber. *J. Atmos. Sci.*, **36**, 1788–1802.
- Schnell, R. C., and G. Vali, 1976: Biogenic ice nuclei. Part I: Terrestrial and marine sources. *J. Atmos. Sci.*, **33**, 1554–1564.
- Starr, D. O'C., and D. P. Wylie, 1990: The 27–28 October 1986 FIRE cirrus case study: Meteorology and clouds. *Mon. Wea. Rev.*, **118**, 2259–2287.
- Stokes, G. M., and S. E. Schwartz, 1994: The Atmospheric Radiation Measurement (ARM) program: Programmatic background and design of the cloud and radiation testbed. *Bull. Amer. Meteor. Soc.*, **75**, 1201–1221.
- Tabazadeh, A., and O. B. Toon, 1998: The role of ammoniated aerosols in cirrus cloud nucleation. *Geophys. Res. Lett.*, **25**, 1379–1382.
- Tränkle, E., and R. G. Greenler, 1987: Multiple scattering effects in halo phenomena. *J. Opt. Soc. Amer.*, **A4**, 591–599.
- Wang, Z., and K. Sassen, 2002: Cirrus cloud microphysical property retrieval using lidar and radar measurements. Part I: Algorithm description and comparison with in situ data. *J. Appl. Meteor.*, **41**, 218–229.
- Workman, E. J., and E. E. Reynolds, 1950: Electrical phenomena occurring during the freezing of dilute aqueous solutions and their possible relationship to thunderstorm activity. *Phys. Rev.*, **78**, 254–259.